





Article

Pavement Distress Estimation via Signal on Graph Processing

Salvatore Bruno ¹, Stefania Colonnese ², Gaetano Scarano ², Giulia Del Serrone ¹
and Giuseppe Loprencipe ^{1,*}

¹ Department of Civil, Constructional and Environmental Engineering, Sapienza University of Rome, Via Eudossiana 18, 00184 Rome, Italy

² Department of Information Engineering, Electronics and Telecommunications, Sapienza University of Rome, Via Eudossiana 18, 00184 Rome, Italy

* Correspondence: giuseppe.loprencipe@uniroma1.it; Tel.: +39-0644585112

Abstract: A comprehensive representation of the road pavement state of health is of great interest. In recent years, automated data collection and processing technology has been used for pavement inspection. In this paper, a new signal on graph (SoG) model of road pavement distresses is presented with the aim of improving automatic pavement distress detection systems. A novel nonlinear Bayesian estimator in recovering distress metrics is also derived. The performance of the methodology was evaluated on a large dataset of pavement distress values collected in field tests conducted in Kazakhstan. The application of the proposed methodology is effective in recovering acquisition errors, improving road failure detection. Moreover, the output of the Bayesian estimator can be used to identify sections where the measurement acquired by the 3D laser technology is unreliable. Therefore, the presented model could be used to schedule road section maintenance in a better way.

Keywords: pavement distress detection; pavement condition index; pavement management program; signal on graph processing; automated distress evaluation systems; Bayesian estimator



Citation: Bruno, S.; Colonnese, S.; Scarano, G.; Del Serrone, G.; Loprencipe, G. Pavement Distress Estimation via Signal on Graph Processing. *Sensors* **2022**, *22*, 9183. <https://doi.org/10.3390/s22239183>

Academic Editors: Maurizio Spadavecchia, Nicola Giaquinto and Francesco Adamo

Received: 12 November 2022

Accepted: 23 November 2022

Published: 25 November 2022

Publisher's Note: MDPI stays neutral with regard to jurisdictional claims in published maps and institutional affiliations.



Copyright: © 2022 by the authors. Licensee MDPI, Basel, Switzerland. This article is an open access article distributed under the terms and conditions of the Creative Commons Attribution (CC BY) license (<https://creativecommons.org/licenses/by/4.0/>).

1. Introduction

1.1. Background

The accurate and reliable assessment of road surface degradation is very important for planning appropriate maintenance strategies, primarily to ensure safety and comfort of the road users. Pavement management systems are the tools traditionally used to assist road managers in decision-making regarding pavement maintenance and rehabilitation; they are mainly based on distress data analysis [1]. According to the World Bank, in fact, the pavement condition of a country's road network determines its economic level [2]. To regulate the activities required to maintain adequate pavement performance, it is essential to gather information on the state of health of the road surface: in this regard, the data can be collected by visual inspections or by automated detection solutions [3].

Visual deterioration inspections have been the most common method used to collect road data for many years: qualified personnel analyze the pavement conditions by walking or traveling in a car at slow speeds [4]. Traditionally, the pavement condition index (PCI) is used to describe the general condition of a pavement section based on road data collected. PCI numerical values, between 0 and 100, allow the road manager to capture useful information about the most suitable intervention techniques to adopt [5]. The ASTM D6433 [6] and ASTM D5340 [7] formalized and standardized the PCI calculation methods. These standards are based on detecting the pavement distress types encountered at the road surface and then on distinguishing each of them by different severity levels. However, the visual surveys are time-expensive, wasteful, and subjective [8].

Therefore, in recent years, automated survey methods have increasingly been employed [9] through innovative and low-cost technologies [10] for the analysis of road pavements, evaluating their potential to improve the automation and reliability of hazard

detection. These automatic methods are safe, fast and repeatable, at the expense of the high cost of the acquisition equipment and the long processing and calculation times [11]. Nondestructive methods of diagnosing the decay of a road surface can include the use of ground-penetrating radar (GPR), laser scanning technology and finite element method (FEM) calculations to evaluate the factors that contribute to early pavement cracks [12].

Most of these methods are pavement crack detection systems based on images [13]: for example, Mataei et al. proposed the structure from motion (SfM) technique in [14], applied on a road pavement, to accurately measure the pavement texture. Du et al. [15] processed the conditions of the road surface, automatically detecting and measuring road discomfort from images based on unmanned aerial vehicles (UAVs). A similar approach was used by Garilli et al. in [16] to detect natural stone pavements, analyzing two supervised classification approaches: the semi-automatic classification plugin for QGIS and a convolutional neural network (CNN). An approach for the automatic detection of raveling [17] was also constructed from image sample processing. A stochastic gradient descent logistic regression (SGD-LR) was subsequently implemented to classify the image samples into two categories of nonraveling and raveling based on a set of extracted characteristics. In the studies [18,19], low-cost data acquisition systems were developed. The systems rely on smartphones equipped with an accelerometer and a geographical positioning system, in one case, and a Sharp IR-based sensor and an accelerometer, in the other, to measure the pavement roughness. To overcome differences coming from dissimilar smartphone sensor properties, an algorithm that uses threshold-based and machine learning approaches for the near real-time detection and the classification of road surface anomalies was proposed in a recent study [20]. Furthermore, the identification, representation, and surface quantification of newly formed holes are important for timely maintenance and repair. This study [21] presents a low-cost based approach for the detection of potholes on asphalt road pavements in urban areas from 2D images using the fuzzy c-means algorithm (FCM). Analyzing the pavement data obtained from 3D laser scanning, meanwhile, an automatic defect detection method was proposed in [22] to simultaneously detect typical cracks and information on deformation defects. Dan and Dan discuss an intelligent approach to the automatic recognition of pavement cracks in [23] based on a two-dimensional amplitude and phase estimation method able to filter low-frequency information. Li et al. proposed the interleaved low-rank group convolution hybrid deep network (ILGCHDN) in [24], with the aim of recognizing cracks and non-cracks on complex road surfaces.

However, it has to be noticed that the output of any data collection system includes errors [25] that may depend on several factors related either to the instrument used to make the measurement or to the personnel performing the action of measuring: researchers around the world have adopted many methods and algorithms to overcome these limits. Dong et al. in [26] summarized and discussed more than 40 data analysis methods useful for investigating raw data coming from pavement detections, including statistical tests, experimental design, regressions, count data model, survival analysis, stochastic process models, supervised learnings, unsupervised learnings, reinforcement learnings, and Bayesian analysis applied in pavement engineering. It can be said that the accurate and reliable estimation of road surfaces is still an open challenge.

1.2. Objectives of the Current Work and Problem Statement

Advanced pavement data collection vehicles (Figure 1), professional range of equipment, represent a modern technique to monitor the road surface conditions over time [27].



Figure 1. A modern data collection vehicle.

In this study, an automated pavement condition data collection using laser crack measurement system (LCMS) [28] was used to identify the distresses detected in some field tests carried out in Kazakhstan [29]. The system works properly under various light conditions (both in sunny and shaded areas), and under low-contrast-intensity conditions, at a driving speed up to 100 km/h [30]. Specifically, it consists of two units, each of which combines a high-power spread line laser with a facing-down high-speed camera in an off-axis configuration, as shown in Figure 2:



Figure 2. LCMS sensors installed on the surveying vehicle.

When combined, the two 3D laser units project a 4 m wide laser line, and its image is captured by the cameras [31]. The pavement data are collected under 1 mm transverse resolution and a depth accuracy of 0.5 mm [32]. A detailed modeling of the 3D road surface is acquired as the surveying vehicle travels along the road using a signal from an odometer to synchronize the sensor acquisition [33]. Based on the output, data post-processing (using specific algorithms within the detection system data processing software) makes it possible, in a single run, to automatically identify the type, severity, and extension of the surveyed distresses [34]. Figure 3 illustrates an example image of a pavement with defects automatically overlaid.

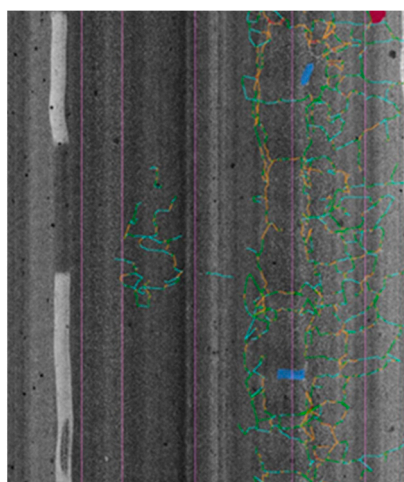


Figure 3. Pavement distress detected (severity = color code).

However, experimental tests have proved that only cracks equal to and greater than 2 mm wide can be effectively detected using 3D laser technology [30]. As a further confirmation of the above, the accuracy of block crack or irregular crack identification has been found better than that of transverse and longitudinal cracks: the latter ones are generally narrower [35]. As for the detection of the transverse cracks, it is less accurate than that of the longitudinal cracks; it is due to the resolution of the laser scanning data, which is higher in the transverse direction than that in the longitudinal direction [22]. Laefer et al. in [36] noted that using laser scanner technology, as the crack width increases, the detection of the crack depth is more accurate. In addition, the accuracy in detecting the crack depth increases as the scanning angle (the offset angle between the crack and the laser scanner) decreases, while it decreases as the scanning distance (the distance between the crack and the laser scanner) increases. In other studies [37], the 3D systems incorrectly reported the joint between the kerb and the pavement as a crack. Detecting sealed cracks is also not easy using LCMS sensors, especially as the sealed crack ages and the sealant wears away and chipping begins [38]. In some field tests on airfield pavements in Ireland [39], a check on the automated distress data outputs showed some problems with the identification of short lengths of hairline longitudinal and transverse cracking and short lengths of low-severity sealed cracks and with the initial misdiagnosis of transverse and diagonal timing as linear cracking. Using deviation analysis of LCMS measurements from manual measurements, Williams et al. in [40] detected some very severe in situ transverse cracks as potholes; moreover, most of the cracking manually measured as longitudinal was reported as meandering/block cracking.

Therefore, the main objective of this study is to solve these limitations and to try to achieve high accuracy in reconstructing noisy or missing real data: a Bayesian estimator of signal on graph has been derived [41].

In particular, we formulate the problem of distress correction as the estimation of a suitably defined signal on graph (SoG), and we propose a novel methodology aimed at correcting possibly altered distress measurements based on the adopted SoG model. The main contributions of the paper are as follows:

- We introduce a novel signal on graph model of the observed distress metrics; specifically, we consider the distress metrics acquired at different spatial sections as signal values associated with the vertices of a graph. The graph edges represent (i) the correlation among different distress metrics at a given spatial section and (ii) the correlation among spatially adjacent measurements of the same metric.
- We derive a novel optimal estimator of the distress metrics. The novel nonlinear Bayesian estimator is built on top of a recent model for signal defined on graphs [42], and it is optimal in the sense that it minimizes the mean square estimation error. In pavement engineering, the Bayesian analysis can be used to obtain and update the

values of parameters based on the historical data and to provide a posterior probability distribution for the parameters [43].

Finally, the PCIs have been calculated based on both raw and processed data in order to compare them and check the accuracy of the Bayesian estimator.

A framework for the pavement distress estimation via SoG processing is shown in Figure 4.

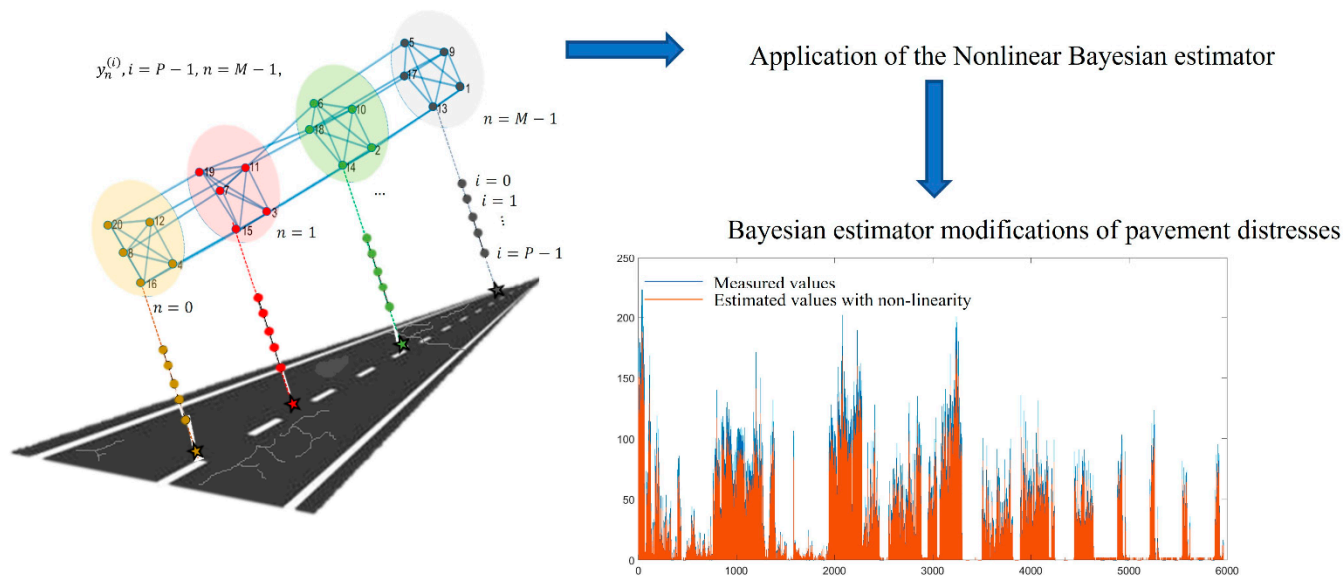


Figure 4. Framework for the pavement distress estimation via SoG processing.

The introduced signal on graph model paves the way for further studies, such as the assessment of the measurement quality as well as the distress feature extraction for deep learning strategies [44].

2. Measurement and Evaluation of Pavement Conditions

The analysis of pavement conditions is a fundamental phase in defining an adequate infrastructure maintenance program, optimizing the budget allocation [45]. The deterioration of a road pavement can be divided into functional and structural characteristics [46]. Functional means that the structure is still efficient, but friction or roughness are compromised, so as to make the movement of vehicles unsafe and uncomfortable; structural, instead, indicates that the pavement shows top-down cracking [47] or other damages (potholes, ruts, etc.) due to repeated traffic loads.

The pavement condition index (PCI) quantifies the current conditions of the pavement considering the type, extent and severity of the detected deterioration in an objective, rational and scientific way. The index is useful for assessing the rate of deterioration, establishing a priority scale of the main maintenance and rehabilitation activities; its calculation procedure is explained in the Standard ASTM D6433 [6] and ASTM D5340 [7], as said in the previous section of this paper. Then, it is a priority to characterize, in terms of both type and severity, the set of distresses on the pavement surface.

The pavement surface degradations analyzed in this paper—among those listed in the standards [6,7]—are those acquired and identified by the LCMS in the field tests: they can be divided into cracks and plastic or viscous surface deformations. Table 1 lists the road surface defects taken into account in the model proposed in this paper; the corresponding descriptions are provided below:

- Alligator cracking occurs in areas subjected to repeated traffic loads. It originates at the bottom of the hot mix asphalt (HMA) layers, where the tensile stress–strain induced by loads is highest. The cracks propagate on to the surface in parallel ways at first,

then interconnect to form polyhedral signs at acute angles, smaller than 60 cm on the longest side;

- Rutting is a road surface depression or groove due to the travel of wheels or skis. The deformation of the asphalt concrete pavement or subbase material can cause the ruts, which can become unsafe during rainy events, when the paths are filled with water;
- Longitudinal and transverse cracking happens lengthwise or crosswise at approximately right angles to the pavement's centerline or laydown direction. These types of cracks are not usually load-associated but can occur, for example, at low temperature or because of asphalt hardening. Nonfilled crack widths less than 6 mm for airport pavement and 10 mm for road pavement are always considered of low severity.
- Block cracks divide the pavement surface into rectangular pieces whose extensions generally range between 0.1 m² and 10 m². They are caused by the shrinkage of the asphalt concrete due to the cyclical variation of daily temperature. Whatever is the load phenomenon, the asphalt manifests an excessive hardening, and so it can occur on non-trafficked sections;
- Raveling is due to the wearing away of the pavement surface with the loss of bituminous material and the consequent dislodging of the aggregate materials. The phenomenon indicates poor quality of the mixture and a hardening of the asphalt binder.
- Lane/shoulder drop-off is the difference in elevation between the traffic lane and the shoulder. Generally, the shoulder settles because of the consolidation or pumping of the underlying material.
- Potholes are bowl-shaped depressions with a diameter less than 1 m on the road surface. The edges are generally sharp, and the sides are vertical. They are formed when small portions of pavement are removed by traffic, and the phenomenon is accelerated by the presence of water that can stagnate inside them.

Table 1. Road surface defects considered in the development of the model proposed in this study.

ID	ASTM Name	Degree of Severity	Unit of Measure	Cause
1		Low	m ²	Load
2	Alligator cracking	Medium	m ²	Load
3		High	m ²	Load
4		Low	m ²	Load
5	Rutting	Medium	m ²	Load
6		High	m ²	Load
7		Low	m	Climatic/Construction defect
8	Longitudinal cracking	Medium	m	Climatic/Construction defect
9		High	m	Climatic/Construction defect
10		Low	m	Climatic/Construction defect
11	Transverse cracking	Medium	m	Climatic/Construction defect
12		High	m	Climatic/Construction defect
13	Block cracking	Medium	m ²	Climatic
14		High	m ²	Climatic
15		Low	m ²	Bituminous mixture low quality
16	Raveling	Medium	m ²	Bituminous mixture low quality
17		High	m ²	Bituminous mixture low quality
18	Lane/Shoulder Drop-off	Medium	m	Climatic/Poor construction
19	Potholes	Low	[-]	Traffic, load

In this table, the ID number identifies the numbering that will recall the single defects in this paper. The absence in Table 1 of block cracking with a low degree of severity is justified by the lack of data on this metric in the totality of the km investigated in the experimental phase.

Once the relevant defects are known, the procedure to calculate the PCI can be implemented [48]. The PCI of each road section is calculated using Equation (1), adding up the total quantity of each type of distress, with its own severity level and density coming

from inspection data. The units for the quantities may be square meters, linear meters, or number of occurrences depending on the distress type. Let P denote the total number of distress types taken into account and m_i denote the number of degrees of severity per the i -th type of distress:

$$PCI = 100 - \sum_{i=1}^P \sum_{j=1}^{m_i} \alpha [T_i, S_j, D_{ij}] \cdot F(t, d) \quad (1)$$

where α is the deduct weighting value depending on distress type T_i , level of severity S_j , and density of distress D_{ij} ; $i = 1, \dots, P$, $j = 1, \dots, m_i$ and $F(t, d)$ is the adjustment factor for multiple distresses, which varies with the total summed deduct value t and number of deducts d .

The PCI of the pavement condition is a numerical value between 0 and 100, where 0 is the worst possible condition and 100 is the best possible condition, as can be observed in Figure 5.



Figure 5. Standard PCI rating scale.

3. Proposed Model of Road Distress Estimation as a Signal on Graph

Herein, we model the automated distress data from the LCMS as signal values measured at the vertices of a graph. Before turning to mathematics, let us outline the association between the road distress measurements and the graph structure. To this aim, let us consider a section in a road lane. For each section (1, 2, ... , n) usually 100 m long and for a total of M sections, a set P of distress metrics (a, b, c, ... , n) is measured by the LCMS. This is exemplified in Figure 6. For each section, distinguished by a different color, we consider as many graph nodes as the number of different measured metrics. The distress metrics are assumed to be correlated to each other. In the section related to the experimental results, we present the results of a preliminary co-occurrence analysis of collected distress data in a suitable measurement set, and we show few metrics to correlate to each other. We represent the correlation between different metrics taken at the same section links between corresponding nodes. Finally, spatially adjacent nodes relative to the same metric are deemed connected, too. This is illustrated in the lower part of Figure 6, where we recognize the constraint graph structures. The total number of nodes is given by the number M of inspected sections times the number P of distresses evaluated by the automated system.

For a useful interpretation, we assume a few metrics to be correlated to each other. The correlation, estimated by means of a preliminary co-occurrence analysis of collected distress data, is represented by links between nodes relative to the same section; see for instance the pairs (1,b) and (1,d). In addition, nodes representing the same metric at adjacent spatial sections are connected as well; see for instance the pairs (1,b) and (2,b). The total number of nodes is given by the number M of inspected sections times the number P of distresses evaluated by the automated system.

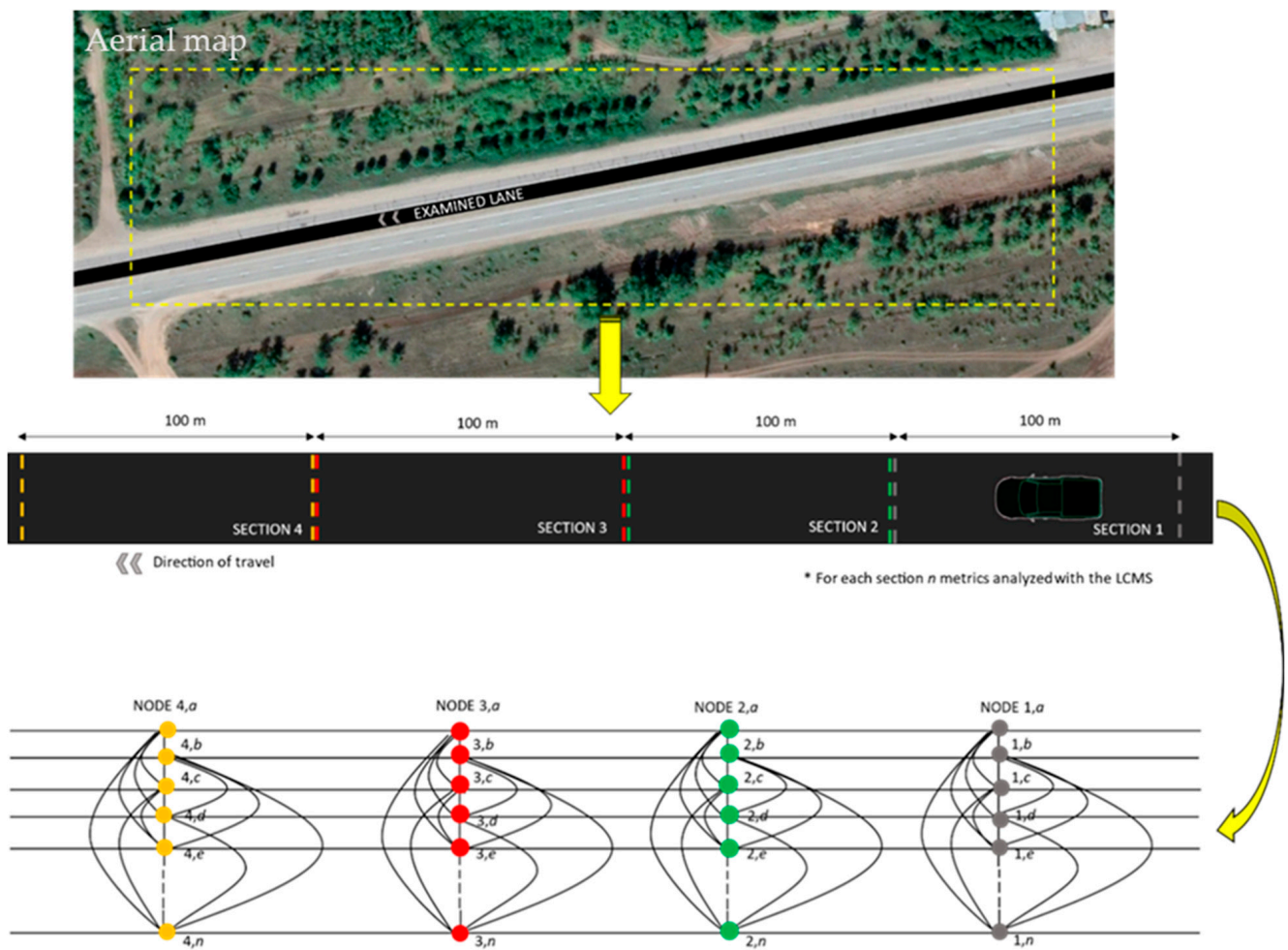


Figure 6. Distress road model as a signal on graph.

With these positions, let us analytically introduce the SoG processing-based model adopted for metric estimation. Formally, let us introduce a graph $G = (V, E)$, where V denotes the set of N vertices and E the set of $N_E \leq N^2$ edges (i.e., real weights) associated with the selected node pairs. The graph connectivity is represented by the $N \times N$ adjacency matrix \mathbf{A} , whose i, j element represents the weight of the edge between the i -th and j -th vertices, as well as by the Laplacian matrix $\mathbf{L} = \mathbf{A} - \mathbf{D}$, \mathbf{D} being the diagonal matrix of the graph node degrees.

The i -th vertex of the graph is associated to a signal x_i , $i = 0, \dots, N - 1$, representing a value acquired at the i -th vertex. Graph G representing the metrics has a particular structure, illustrated in Figure 6 (bottom): The elementary graph connectivity representing the metric correlation at a given spatial section is replicated at different sections; moreover, the corresponding vertices representing the same metric at adjacent spatial sections are connected. This structure is the result of a product of graphs, as exemplified in Figure 7 for the toy case of $P = 5$ metrics measured at $M = 4$ investigated sections. The graph in Figure 7a represents the similarity between metrics at a given section, the path graph in Figure 7b represents the similarity between the same metric over adjacent spatial sections and Figure 7c represents the overall product graph. For a product graph G , the Laplacian matrix \mathbf{L} is analytically found as the Kronecker sum of the Laplacian of the elementary graphs G_1, G_2 as: $\mathbf{L} = \mathbf{L}^{(1)} \oplus \mathbf{L}^{(2)}$.

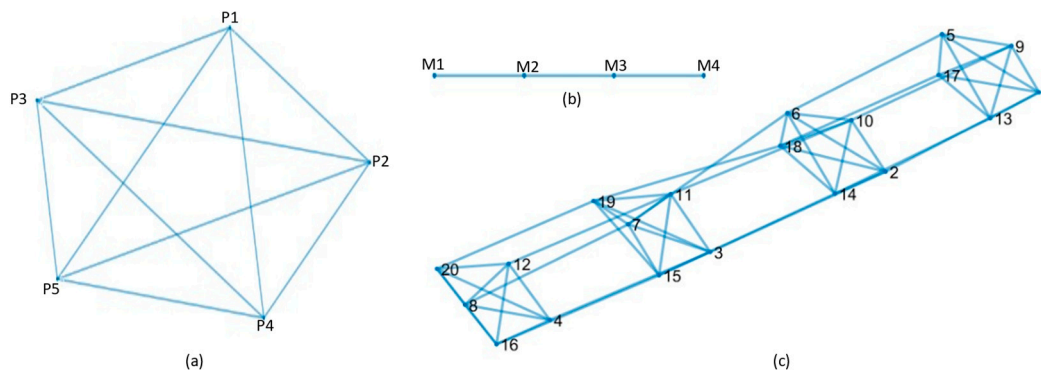


Figure 7. Product of graphs example for the toy case considering $P = 5$ metrics (P1, P2, P3, P4, P5) measured at $M = 4$ sections (M1, M2, M3, M4): (a) graph of the metrics' correlation at a given section); (b) path graph representing the similarity of the same metric over adjacent spatial sections; (c) overall product graph.

For the case under concern, graph G_1 models the similarity between the P metrics. The adjacency matrix coefficients $a_{ij}^{(1)}$, $i, j = 0, \dots, P - 1$ are calculated according to Equation (2) as the correlation coefficients between the i -th and j -th distress metric values, namely

$$a_{ij}^{(1)} = \frac{\sum_n y_n^{(i)} y_n^{(j)}}{\sqrt{\sum_n (y_n^{(i)})^2} \sqrt{\sum_n (y_n^{(j)})^2}} \quad (2)$$

where $y_n^{(i)}$ and $y_n^{(j)}$ are the possibly noisy measured values of the i -th and j -th distress metrics on $n = 0, \dots, M - 1$ road sections, centered with respect to their mean and normalized to unitary variance. Graph G_2 models the similarity between spatially adjacent samples of the same metric. The adjacency matrix coefficients $a_{ij}^{(2)} = 1$ if $|i - j| = 1$ and 0 otherwise. From a computational complexity point of view, let us observe that when the number P of measurements is large, the computation of the Kronecker sum is heavy, and it can be avoided by suitably managing the sparse adjacency matrices.

4. Nonlinear Bayesian Estimation of the Road Distress

Stemming from the above settings, we herein introduce the model of the noisy observed distress metrics in order to derive a Bayesian estimator of noisy or missing measurements. Bayesian estimation exploits a priori knowledge on the data to be recovered, typically in the form of probabilistic priors, and it is of paramount importance in real-world data modeling due to its ability to conjugate the prior statistical model with the information pertaining the observed data [49]. Herein, we derive the Bayesian estimator in closed form. Its computation does not require a training stage leveraging a large annotated dataset as it occurs in supervised machine learning techniques such as linear and nonlinear regression or decision trees [50–52]. On the contrary, the Bayesian estimator leverages few model parameters (e.g., data mean and variance) that can be straightforwardly estimated on the data.

In the following, we introduce the main notation and the definition of the Bayesian estimator as the optimal nonlinear estimator from the point of view of the square of the error. Then, we derive its analytical formulation in closed form.

The set of P measurements acquired at M different road sections $y_n^{(i)}$, $i = 0, \dots, P - 1$, $n = 0, \dots, M - 1$ is modeled as shown in Equation (3):

$$y_n^{(i)} = x_n^{(i)} + w_n^{(i)}, \quad i = 0, \dots, P - 1, \quad n = 0, \dots, M - 1 \quad (3)$$

where $x_n^{(i)}$ is the ground truth signal on graph representing the actual distress and $w_n^{(i)}$ is independent additive noise modeling the error of the acquisition system. Let us observe

that the underlying graph model allows us to associate to each measurement $y_n^{(i)}$ a set $S_n^{(i)}$ of v neighboring measurements, either referred to the same road section or to spatially adjacent ones. With these positions, we leverage the knowledge of the v neighboring measurements in $S_n^{(i)}$ to improve the estimate the ground-truth value $x_n^{(i)}$. According to Bayesian estimation theory, the optimal minimum mean square error (MMSE) estimator of $x_n^{(i)}$, given the measured value $y_n^{(i)}$ and the v neighboring measurements in $S_n^{(i)}$, is computed as the following expected value (Equation (4)):

$$\hat{x}_n^{(i)} = \mathbb{E} \left\{ x_n^{(i)} \mid y_n^{(i)}, y_t, t = 1, \dots, v; y_t \in S_n^{(i)} \right\} \quad (4)$$

where, without a loss of generality, we have compactly denoted the measurements in $S_n^{(i)}$ as $y_t, t = 1, \dots, v$.

In order to compute the above expectation, we model the true distress metric $x_n^{(i)}$ resorting to a recently introduced probabilistic model [42], which allows us to compactly account for the correlation between metrics measured at graph vertices. Stemming from the model in [42], herein we consider the following probability density function of the generic ground truth metric x conditioned to the ground-truth neighboring values $x_i, i = 1, \dots, v$ as defined in Equation (5):

$$p_{X|X_1 \dots X_v}(x|x_1 \dots x_v) = p_0 \delta(x) + p_1 K e^{-\sum_{i=1}^v \beta_i (x-x_i)^2} \quad (5)$$

where we assume that with probability p_0 , the observed distress metric is zero valued, and with probability $p_1 = 1 - p_0$, it obeys to the Markovian signal on the graph model. The parameter K is a normalization factor and the parameters $\beta_i, i = 1, \dots, v$ weight the similarity of the current metric x with the neighboring ones $x_i, i = 1, \dots, v$.

In the following, a few rules of thumb for setting the probability density function parameters will be illustrated. We assume the observation noise to be normally distributed, so that the observed metric $y_n^{(i)}$ is related to the ground truth metric $x_n^{(i)}$ by the following conditional density function (Equation (6)):

$$p_{Y|X}(y|x) = \frac{1}{\sqrt{2\pi}\sigma_W} e^{-\frac{(y-x)^2}{2\sigma_W^2}} \quad (6)$$

With these positions, the optimal minimum mean square error estimator of the considered metric, i.e., the expected value in (3), is derived in closed form by extending the algebraic approach adopted in [53] with the application of blind equalization and in [54] with the application of multichannel image deconvolution. For the sake of compactness, we omit the details here and come up with the final formula, which nicely blends the noisy measure y and the signal values in the neighbor set $S_n^{(i)}$ to provide the optimal estimate.

The optimal MMSE estimator \hat{x} in (4) is computed as defined in Equation (7):

$$\hat{x} = \frac{\mu_1}{1 + \frac{1}{K} \frac{p_0}{1-p_0} \exp\{-(\mu_2 - \mu_1^2) \sum_{i=1}^v \beta_i\}} \quad (7)$$

where

$$\mu_1 = \frac{\beta_0 y + \sum_{i=1}^v \beta_i x_i}{\sum_{i=1}^v \beta_i}, \quad \mu_2 = \frac{\beta_0 y^2 + \sum_{i=1}^v \beta_i x_i^2}{\sum_{i=1}^v \beta_i}$$

represent the linear and quadratic weighted averages.

In Equation (7), we recognize that \hat{x} is a nonlinear function of the noisy observation y and of its neighboring values. For given known values in the neighboring nodes, the Bayesian estimator \hat{x} is a nonlinear function of y , namely $\hat{x} = \eta(y)$. The action of the nonlinearity $\eta(y)$ is exemplified in Figure 8, which plots \hat{x} versus y for assigned neighboring values and where we highlight the nonlinearity action for the case of a measured value y equal to 6.2 and observed

neighboring values equal to 2.7, 2.9, 2.9, 3.3, and 3.4. In Figure 8a, we consider a constant value of the parameter β_0 , and then we consider various values of p_0 . The extent of the attenuation effect of the nonlinear estimator on small y values varies with the a priori probability p_0 of zero-valued distress metrics; in addition, the observation is corrected to result in line with the neighboring values. In Figure 8b, we consider a constant value for p_0 and various values of β_0 , representing the quality of the measurement y . For a much-degraded observation, i.e., $\beta_0 = 0$, the nonlinear estimator boils down to a constant determined by the neighboring values only. For increasing quality, the nonlinear estimator tends to leave the observation unaltered.

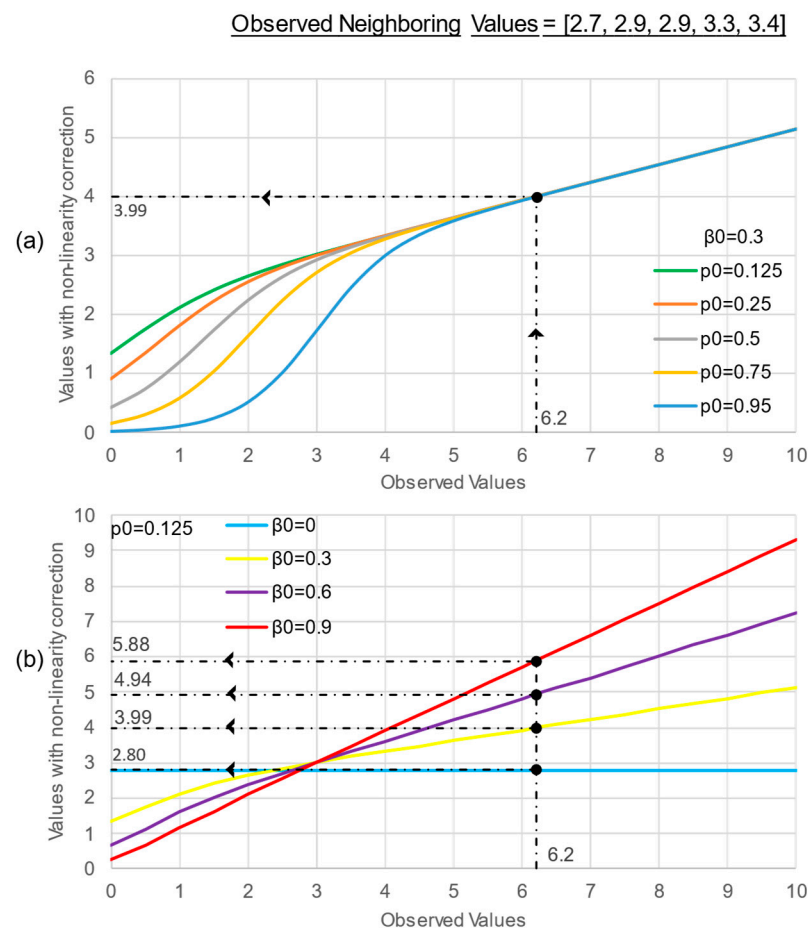


Figure 8. Effect of the nonlinear estimator on the observed value as the p_0 (a) and the β_0 parameter (b) change; the case of observed value equal to 6.2 is highlighted.

In summary, the observed value, with a statistical nature of its own (it could be zero or related to its neighbors), is corrected according to the formulated aprioristic hypothesis, as expressed by the parameters of nonlinearity. In particular, the β_0 parameter represents the hypothesis of accuracy of the observed data: As β_0 tends to the unit value, we have higher confidence in the input data, and therefore, the lower is the correction made by the nonlinearity. As regards p_0 , it provides information related to the expectation of having zero values in measurements: As p_0 tends to the unit value, the hypothesis that the ground truth value is equal to zero becomes prominent.

In the following section, we apply the proposed signal on graph model and the associated Bayesian estimation procedure to real road distress measurements.

4.1. Performance of the Bayesian Estimator for the Toy Case

To this aim, we consider the graph in Figure 7c, and we associate with each of the $P = 5$ metrics a set of $M = 4$ sections.

Herein we illustrate the performance achieved by the Bayesian estimator on road data when they are affected by additive acquisition noise. Firstly, we consider the graph in Figure 7c, modeling the acquisition of $P = 5$ metrics over $M = 4$ sections $x_n^{(i)}$ ($i = 0, \dots, P - 1, n = 0, \dots, M - 1$) selected by the road dataset considered in this research work. Then, the observation $y_n^{(i)}$ is obtained from $x_n^{(i)}$ by adding white noise; for concreteness sake, we consider normally distributed noise, typically used to model the superposition of different random contributions [55], with signal to noise ratio SNR= 5 dB. Therefore, we compute the above-described Bayesian estimator $\hat{x}_n^{(i)}$ to each graph vertex, obtaining the set of restored values.

To assess the ability of the Bayesian estimator in recovering the data, we compute the achieved mean square error (MSE) defined as follows (Equation (8)):

$$MSE = \frac{1}{MP} \sum_n \sum_i \left(x_n^{(i)} - \hat{x}_n^{(i)} \right)^2 \quad (8)$$

We average the MSE over 10 Montecarlo runs and plot the result in Figure 9 (“Bay” bar). For comparison sake, we consider different linear and nonlinear estimators [56,57], namely the mean and median of spatially adjacent measurements (“Mean”, “Median”), which are optimal in that they minimize the mean square or the mean absolute error for suitable kinds of noisy measurements. In principle, also the successive convex approximation (“SCA”) signal estimator in [42], which minimizes the mean square error of the estimate subject to a smoothness regularization constraint, could be considered. Still, since the SCA estimator poses a computational challenge over huge datasets such as the real roads datasets considered in this study, we resort to an over-regularized version of the SCA estimator, which is obtained by averaging the observations over the neighboring values over the considered graph (“Graph”). The abovementioned methods do not require large human annotated training datasets but only a global statistical characterization that is feasible for acquiring in practical applications. The results in Figure 9 show that the Bayesian estimator outperforms the competitors in terms of achieved MSE.

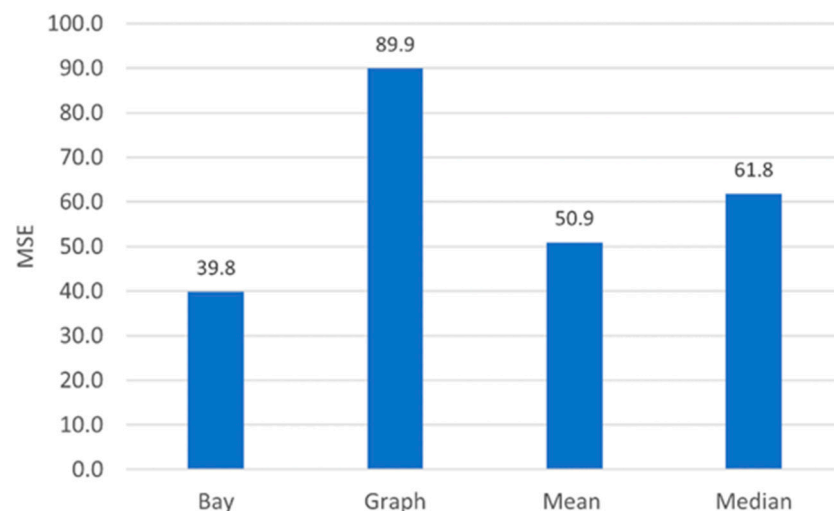


Figure 9. $P = 5$ metrics, $M = 4$ sections graph schematically represented in Figure 6. MSE of the Bayesian estimator (Bay), the linear estimate obtained averaging over neighboring graph vertices (Graph), the linear estimate obtained averaging over spatially adjacent vertices (Mean) and the nonlinear estimate obtained as the median over spatially adjacent vertices (Median).

5. Application of the Proposed Model to Real Data

Without the loss of generality, this research was conducted using pavement data collected within the road network of the Republic of Kazakhstan; in particular, 2468 km of flexible pavements along highways (Figure 10 and Table 2) were surveyed. The type, severity, and extension of the distresses were measured with the Pavemetrics® Laser Crack

Measurement System (LCMS[®]), considering subsections 100 m long for a total number of sample units equal to 24,680. It has to be noticed that the application of this pavement distress estimation via Signal on Graph processing could be extended to every road network whose distress data are known regardless of the surveying technique adopted.

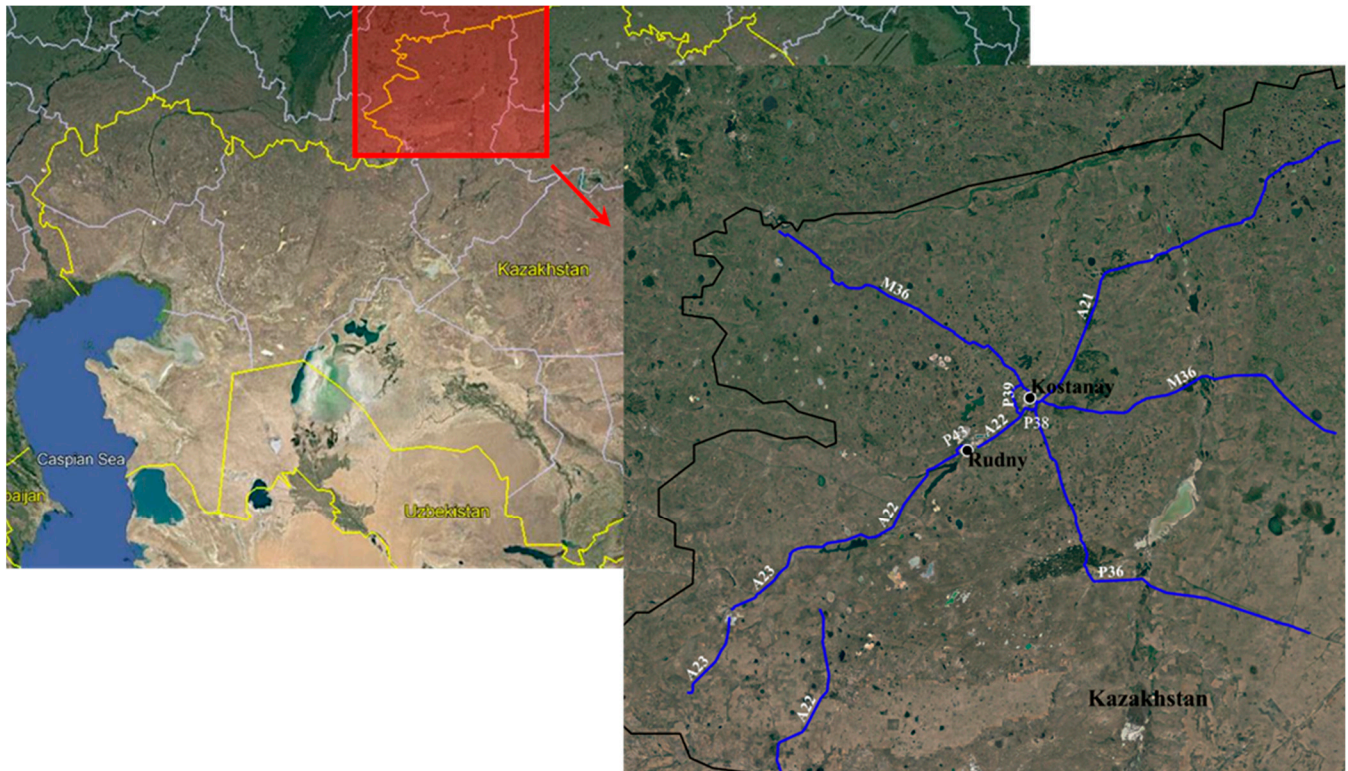


Figure 10. Examined roads—2468 km.

Table 2. Road surface defects considered in the development of the model proposed in this study.

Road Name	Category	Direction
M36	International Highway	Border of Russia—Kostanay—Astana—Karaganda—Almaty
A21	National Highway	Mamlyutka—Kostanay
A22	National Highway	Karabutak—Komsomol’skoe, Kazakhstan—Denisovka—Rudny, Kazakhstan—Kostanay
A23	National Highway	Denisovka—Zhetikara—Muktikol
P36	Regional Highway	Kostanay—Auliekol—Surgan
P38	Regional Highway	Kostanay Southern Bypass (At Minchurinskoe)
P39	Regional Highway	Kostanay Western Bypass
P43	Regional Highway	Rudny West Bypass

In order to be able to evaluate the performance of the proposed model, the available dataset was split into two subsets of measurement sections: a training set (calibration phase) and a test set (validation phase), in the ratio approximately 75:25. Specifically, data collected along the A22 national highway were chosen as the test set, because of its 596 km length for a total number of sample units (called “Section Number” in the abscissa axis of the diagrams) equal to 5960, which represent 25% of the total road network length. The other roads were used as the training set, belonging to the same road class type. The training set was used to calculate the correlation matrix related to the investigated metrics, while the test set was used after the training to evaluate the model performance on unseen data. For these data, the model proposed in this paper was particularized as follows.

5.1. Construction of the Graph of the Metrics

The adjacency matrix coefficients $a_{ij}^{(1)}$, $i, j = 0, \dots, P - 1$ were calculated as the correlation coefficients between the i -th and j -th distress metric values. Figure 11a illustrates, in pseudocolor, the adjacency matrix coefficients $a_{ij}^{(1)}$, $i, j = 0, \dots, P - 1$ of the graph of the metrics. To reduce the metric graph complexity, and hence the computational burden, the adjacency matrix was thresholded by setting to zero the coefficients lower than 0.1. The considered thresholded adjacency matrix is shown in Figure 11b.

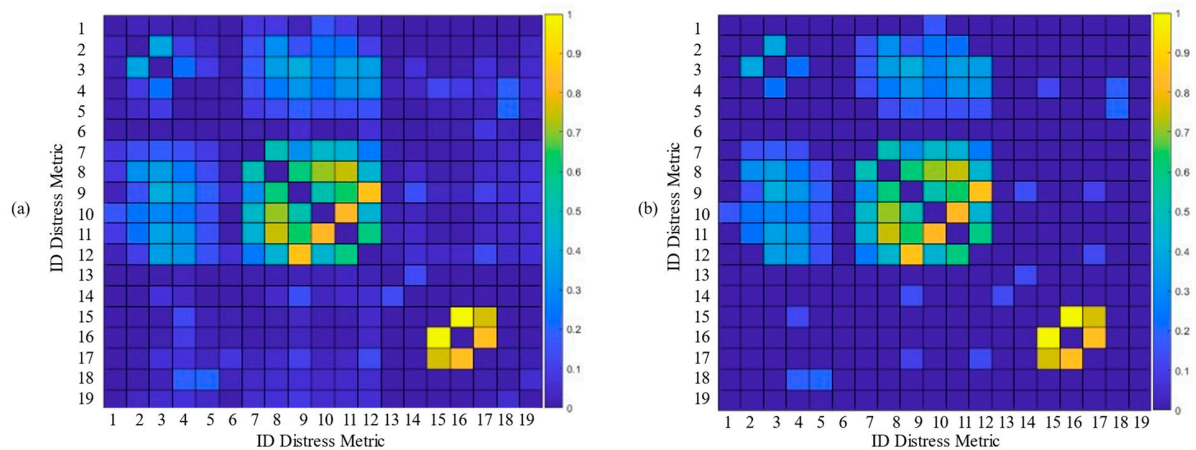


Figure 11. Adjacency matrix coefficients $a_{ij}^{(1)}$, $i, j = 0, \dots, P - 1$ of the graph of the metrics, calculated as the correlation coefficients between the i -th and j -th distress metric values: (a) original values and (b) thresholded values with threshold $\vartheta = 0.1$.

From Figure 11, we recognize that the most correlated metrics are those (i) at indexes 15, 16, 17, corresponding to different levels of raveling (see Table 1), and (ii) at indexes 8, 11 and 9, 12, corresponding to medium and high levels of longitudinal and transverse cracking, respectively. A smaller correlation effect is found between metrics 2–4, related to alligator cracking, and the metrics 10–12, representing transverse cracking.

With these positions, we illustrate in Figure 12 the graph of the metrics as estimated on the training data. The i -th node represents the i -th metric; the i -th node size is proportional to the node degree, which is computed as the sum of the weights of the node's edges, namely $\sum_{j=0}^{P-1} a_{ij}$, $i = 0, \dots, P - 1$. The degree allows for identifying relevant, highly correlated metrics. Let us observe that the correlation of some road surface defects (namely ID 1, 13, and 14) with other cracks may be underestimated since these metrics were detected on few surveyed road sections, corresponding to less than 0.1% of the total number of sections. Moreover, it is possible to observe from Figure 12 that the metrics, namely ID 1, 6, 13, 14, and 18, are not correlated between them.

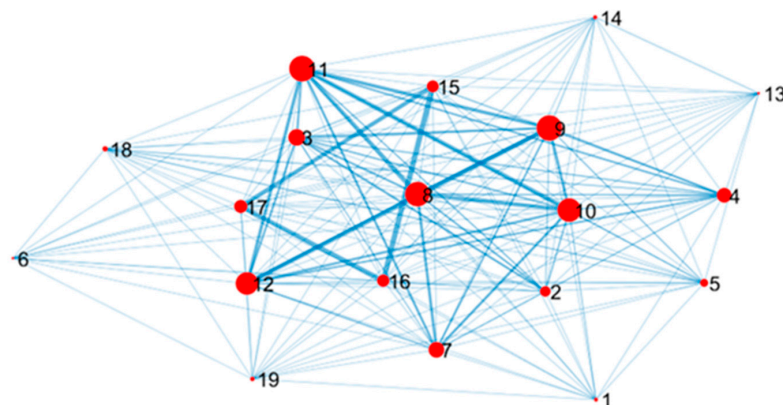


Figure 12. Correlations between the different investigated metrics.

5.2. Construction of the Path Graph on Adjacent Spatial Sections

According to the above-described path graph model, each measurement is linked to the previous and following ones. In practice, when computing nonlinearity, the values assumed by the metric in the spatially neighboring sections are substituted by the averages over the five previous and next inspected sections. This operation averages out possible noise affecting the measurement.

In summary, to correct the generic value $y_n^{(i)}$, the neighboring values over the nearest spatial sections are considered, as well as the correlated metrics. This is shown in Figure 13, where the black square represents the current metric $y_n^{(i)}$, the blue squares represent the correlated metrics acquired at the same section, and the yellow ones represent the spatially neighboring measurements averaged out to compute the spatial neighborhood estimates.

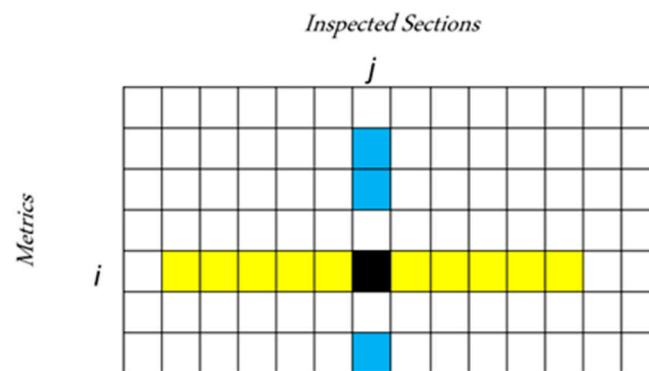


Figure 13. Measurements involved in the estimation of the i -th metric at the n -th inspected section (black square): measurements relative to correlated metrics at the same inspected section (light blue squares), and measurements of the same metric averaged over spatially adjacent sections (yellow squares).

A further remark about the metrics' ranges is in order. Although being correlated, the measurements corresponding to different metrics span different ranges. According to the information in Table 1, Figure 14 shows the maximum measured values for each of the metrics, as computed on the test dataset. Before processing the measurements by the nonlinear estimator, they are normalized with respect to their maximum value. This operation prevents numerical errors and simplifies the selection of the $\beta_i, i = 1, \dots, \nu$ parameters. The result of the metric normalization is shown in Figure 15, which represents in pseudocolors the PxM matrix of the measurements.

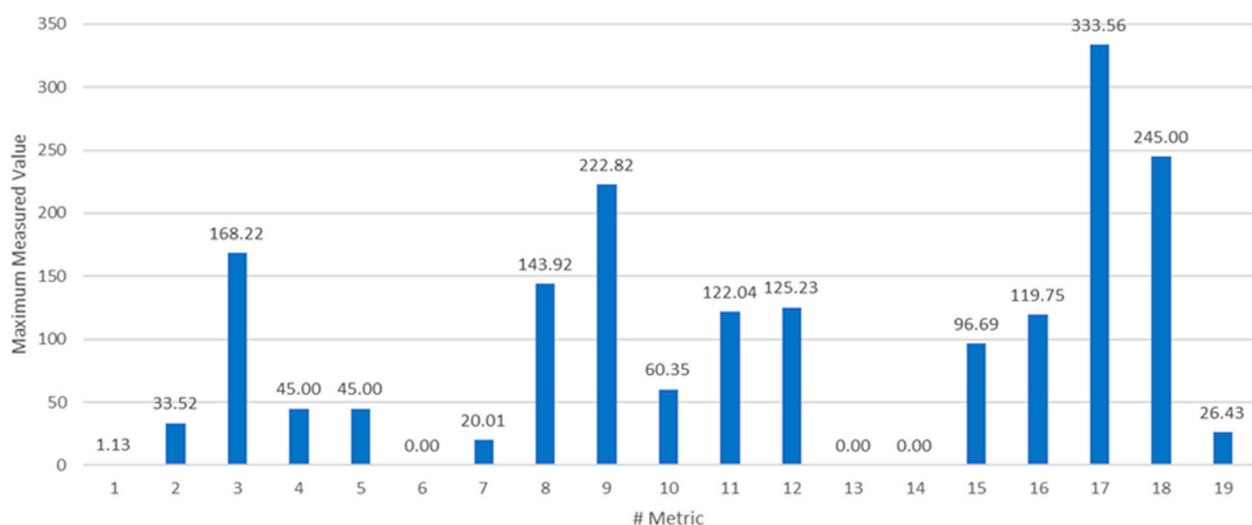


Figure 14. The maximum measured values for each of the metrics.

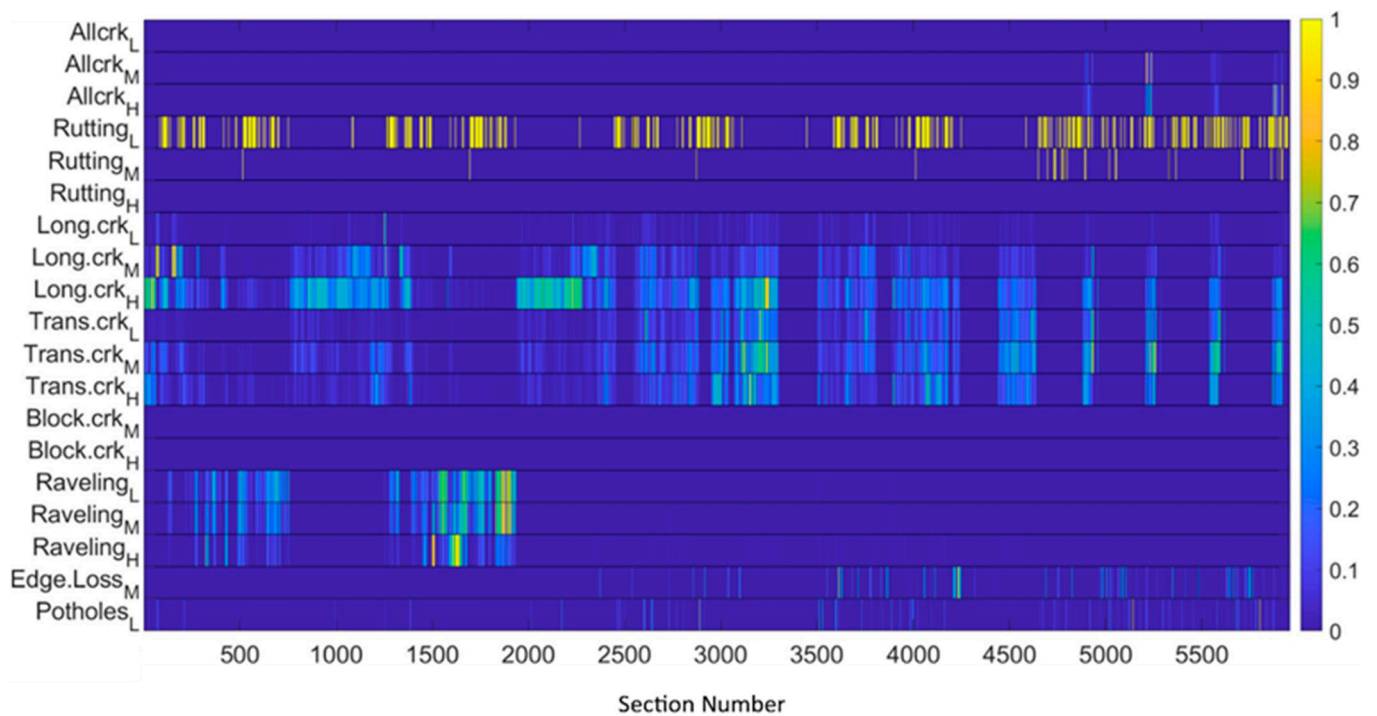


Figure 15. Metrics normalized to the maximum measured values.

6. Experimental Results

In this section, we illustrate the application of the Bayesian estimator to real data metrics. Specifically, we assume that the metrics are affected by generic acquisition noise, and we prove that they are corrected by the estimator. The nonlinearity parameters p_0 and β_0 are assigned values of 0.1 and 0.8, respectively. Regarding the assignment of the β_0 parameter value to 0.8, it reflects the hypothesis of good accuracy in the observed data. The value attributed to p_0 is in accordance with the high degree of confidence in the LCMS technology in detecting defects. It should be noted that the proposed method could also be applied considering data collection methods with less accuracy than those of the LCMS, defining lower values of the parameter β_0 . Herein, we aim at assessing the performance of the model for various real pavement distresses.

Firstly, in order to quantitatively assess the ability of the estimator to recover from possible acquisition noise, we reproduce the experimental conditions as in Section 4.1, and we evaluate the MSE achieved by the proposed estimator and its competitors. The results are reported in Figure 16. We recognize that in this simulated environment, the random fluctuations due to the additive noise are reduced up to 25% with respect to the competitors. Thereby, the estimator is able to correct pseudo-random fluctuations by exploiting correlation among different metrics as well as among adjacent spatial locations.

Given this initial performance assessment, we now analyze the effect of the Bayesian estimator acting on the LCMS raw data. To this aim, we apply the estimator to each measured value, apart from the distress known as rutting (#4, 5 and 6), which assumes binary standard values, namely 0 or 45 m². For this binary metric, the optimal nonlinearity slightly differs from that in (7), and following the approach in [54], it can be demonstrated to take the form of a soft thresholding stage. This notwithstanding, the values for the rutting metric are taken into account to adjust the values of the metrics that are sufficiently correlated with it.

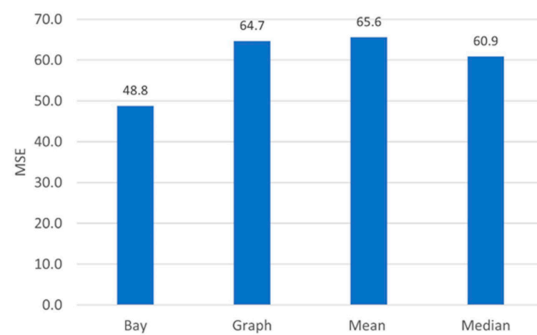


Figure 16. Test Set. MSE of the Bayesian estimator (Bay), the linear estimate obtained averaging over neighboring graph vertices (Graph), the linear estimate obtained averaging over spatially adjacent vertices (Mean) and the nonlinear estimate obtained as the median over spatially adjacent vertices (Median).

In Figure 17, we report the road distress measurements $y_n^{(i)}$ (blue dots), and the outputs of the Bayesian estimator $\hat{x}_n^{(i)}$ (orange dots). The single defects are represented, and the units of measurement are defined in Table 1; the measured values and the values replaced with the nonlinearity are compared: for the sake of clarity, a distress metric, namely the longitudinal cracking (Long.crk_H), is displayed in a larger scale.

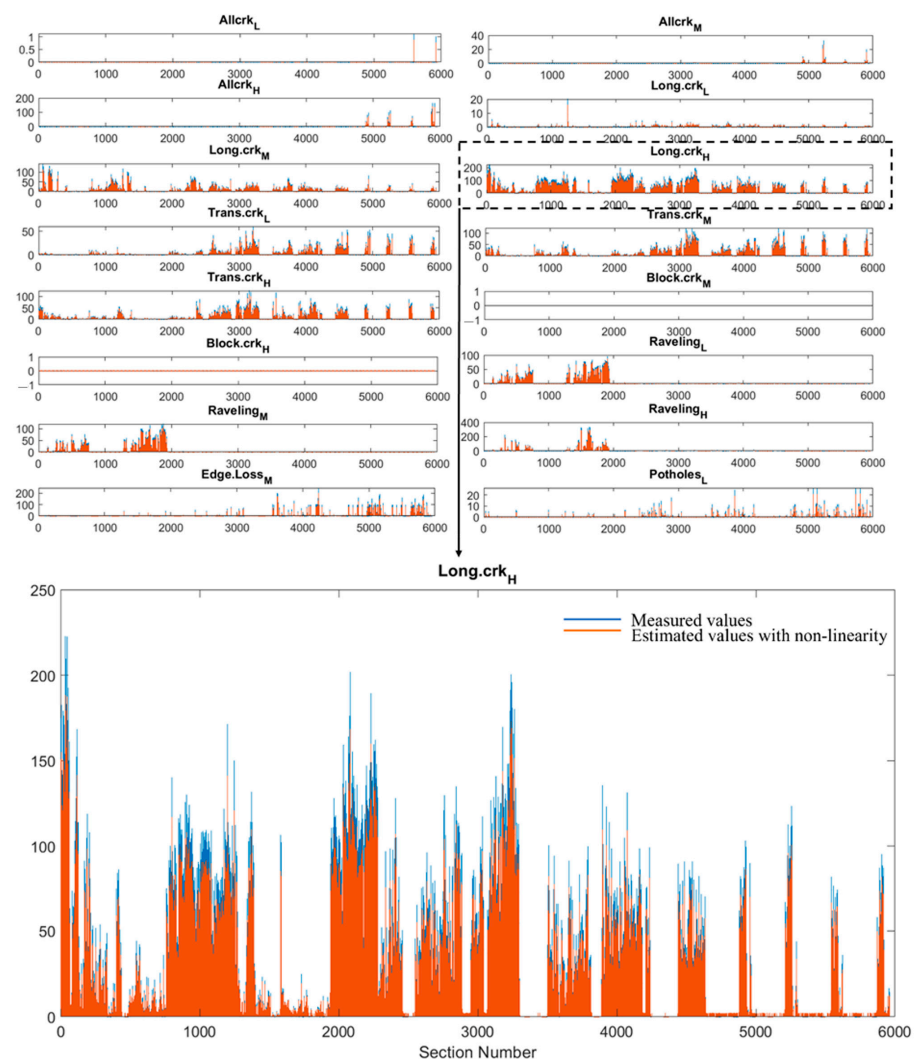


Figure 17. The measured values (blue) and the estimated values with nonlinearity (orange) for each of the metrics.

In order to make it easier to read the results, the difference between the measured starting values and the estimated values with the nonlinearity was also calculated section by section (Figure 18). We recognize that metrics characterized by large values, as for instance Long.crk_H, lead to larger numerical differences between the LCMS measured values and the estimated values with nonlinearity counterparts; this explains the larger differences spotted in Figure 18 for this metric. In summary, it is easy to detect the sections where the substitution of the values applying the proposed model has generated remarkable differences. The problem of identifying sections where the 3D laser technology can make mistakes is a highly attractive problem: the approach discussed in this paper may thus be a solution.

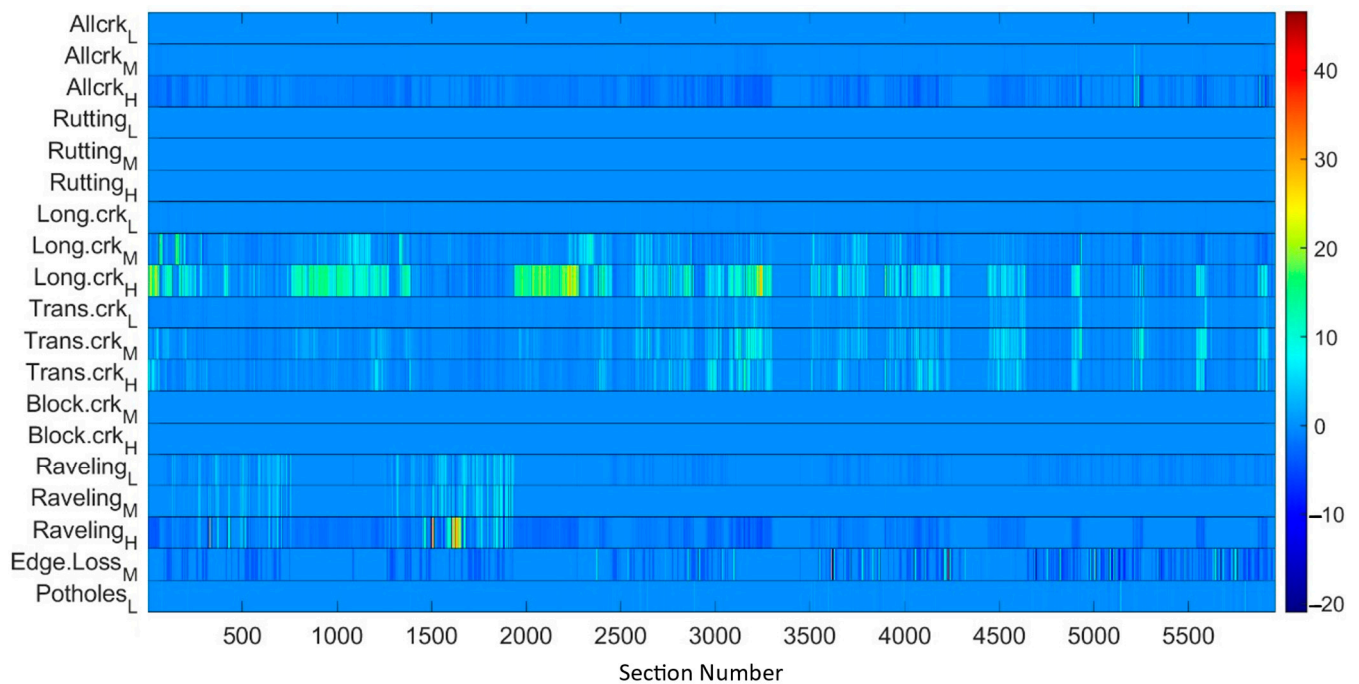


Figure 18. The difference between the measured values and the estimated values with non-linearity.

Finally, we discuss the effect of the metric at the output of the Bayesian estimator on the PCI index. It should be noted that a numerical variation of the value of the single defect turns nonlinearly into the evaluation of the PCI index. For the above-described measurements, the PCI has been calculated with the implementation of a Visual Basic for Application (VBA) language-based program with interpolation by the parametric cubic spline of all of the density/deduct value curves of ASTM D6433 distress types [58], both in the case of the values measured with the LCMS and in the case of the values at the output of the Bayesian estimator. In particular, the variation of the PCI between the measurements and their processed version was statistically analyzed. Figure 19a,b plot the histogram and the cumulative density function of the PCI correction due to the adoption of the Bayesian estimator. As shown in Figure 19, the Bayesian estimator modifies the estimated PCI, and there are drastic changes in the estimated PCI values in only a few sections, where indeed the proposed signal on graph approach improves the quality of the LCMS measurements. Moreover, it can be observed that approximately for the 80% of the sections a lower PCI is returned by adopting the nonlinear approach: this result is in accordance with the study by Mulry et al. [39], which shows how the manually measured PCI is lower than the LCMS PCI.

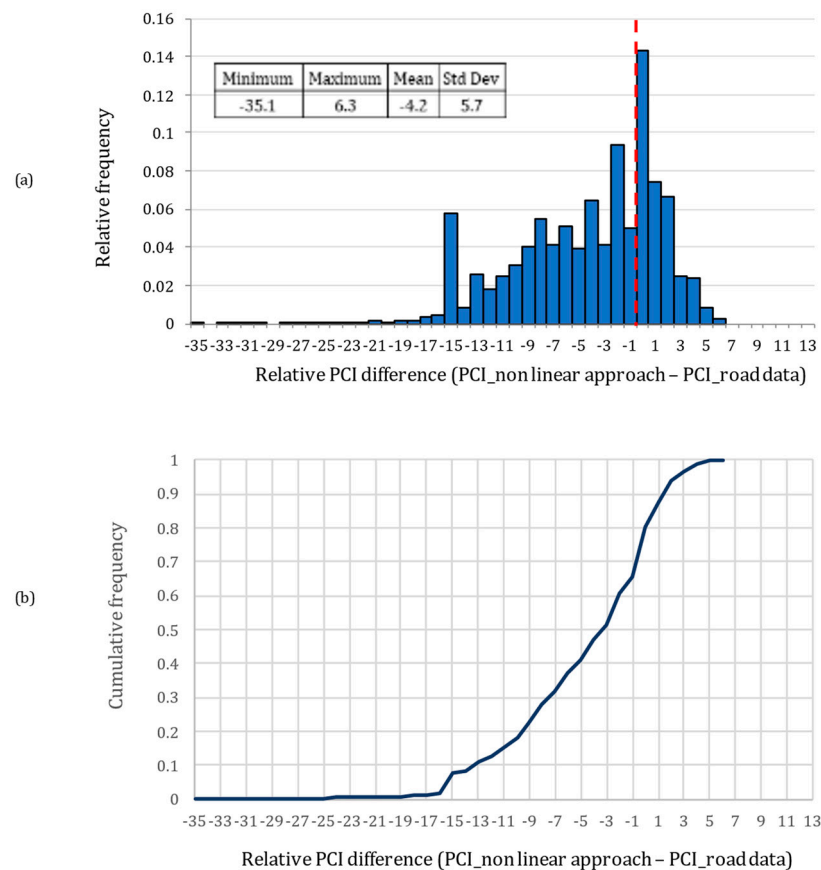


Figure 19. PCI correction due to Bayesian estimator in terms of relative frequency (a) and cumulative frequency (b).

7. Conclusions and Future Works

In this paper, we have introduced a novel Signal on Graph model of pavement distress metrics, by associating the values of the distress metrics acquired at different spatial sections to the vertices of a graph. The graph represents the correlation between different distress metrics at a given spatial section and the correlation among spatially adjacent measurements of the same metric. Then, we have derived a novel Bayesian estimator of the distress metrics, built on top of a recent model for signal defined on graphs. The estimator does not require large training annotated dataset, as linear and nonlinear regression techniques, since it leverages few parameters (mean, standard deviations) straightforwardly estimated from the observed data. Without loss of generality, we have assessed the methodology performance on a wide dataset of distress values, detected in some field tests carried out in Kazakhstan. The results can be summarized as follows:

- The related Bayesian estimator is effective in recovering acquisition errors, achieving an overall reduction of the error mean square value of about 25%, with respect to the considered competitors;
- The proposed methodology can be employed to identify sections where the measurements acquired by the 3D laser technology are unreliable related either to the limitations of the automated data collection or data processing software, as extensively discussed in the Introduction section. Indeed, a failure in the measurement system could be revealed when a large difference is computed at the same section between the observed value and the restored one obtained by the Bayesian estimator, i.e., the likelihood of the measured value is small;
- The proposed signal on graph approach selectively improves the quality of the LCMS measurements, as the Bayesian approach achieves a better accuracy in the PCI estimation compared to the LCMS PCI.

The herein presented signal on graph model of distress metrics can be applied independently on the acquisition method and it is viable for important developments. Firstly, the model naturally extends to account for side graph node information, such as scheduled road section maintenance or historical records. The graph-based structure also seamlessly encompasses Geographic Information System (GIS). Furthermore, the Bayesian estimator based on the signal on graph model of the distress measurements can be employed as a robust feature extraction stage at the input of a Deep Learning based pavement distress estimation system, leading to robust and accurate data-driven PCI estimation.

Author Contributions: Conceptualization, G.L. and S.C.; methodology, S.B. and S.C.; software, S.B. and S.C.; validation, G.L., S.B. and G.D.S.; formal analysis, G.L. and S.C.; investigation, S.B. and G.D.S.; resources, G.L.; data curation, S.B. and G.S.; writing—original draft preparation S.B., S.C. and G.D.S.; writing—review and editing, G.L. and G.S.; visualization, S.B. and G.D.S.; supervision, G.S.; project administration, G.L. All authors have read and agreed to the published version of the manuscript.

Funding: This research was developed within the grant number RM120172B05C0B39, title “Urban pavement monitoring system using car and bike/scooter sharing vehicles” financed by the Sapienza, University of Rome.

Institutional Review Board Statement: Not applicable.

Informed Consent Statement: Not applicable.

Data Availability Statement: The data presented in this study are available on request from the corresponding author. The data are not publicly available due to confidentiality reasons.

Conflicts of Interest: The authors declare no conflict of interest.

References

1. Cafiso, S.; Di Graziano, A.; Goulias, D.G.; D’Agostino, C. Distress and Profile Data Analysis for Condition Assessment in Pavement Management Systems. *Int. J. Pavement Res. Technol.* **2019**, *12*, 527–536. [\[CrossRef\]](#)
2. Queiroz, C.A.; Gautam, S. *Road Infrastructure and Economic Development: Some Diagnostic Indicators*; World Bank Publications: Washington, DC, USA, 1992; Volume 921.
3. Ragnoli, A.; De Blasiis, M.; Di Benedetto, A. Pavement Distress Detection Methods: A Review. *Infrastructures* **2018**, *3*, 58. [\[CrossRef\]](#)
4. Bruno, S.; Vita, L.; Loprencipe, G. Development of a GIS-Based Methodology for the Management of Stone Pavements Using Low-Cost Sensors. *Sensors* **2022**, *22*, 6560. [\[CrossRef\]](#) [\[PubMed\]](#)
5. Hafizyar, R.; Mosaberpanah, M. Evaluation of Flexible Road Pavement Condition Index and Life Cycle Cost Analysis of Pavement Maintenance: A Case Study in Kabul Afghanistan. *Int. J. Sci. Eng. Res.* **2018**, *9*, 1909.
6. D6433–20; Standard Practice for Roads and Parking Lots Pavement Condition Index Surveys. ASTM International: West Conshohocken, PA, USA, 2020.
7. D5340–20; Standard Test Method for Airport Pavement Condition Index Surveys. ASTM International: West Conshohocken, PA, USA, 2020.
8. Fan, Z.; Lin, H.; Li, C.; Su, J.; Bruno, S.; Loprencipe, G. Use of Parallel ResNet for High-Performance Pavement Crack Detection and Measurement. *Sustainability* **2022**, *14*, 1825. [\[CrossRef\]](#)
9. Cafiso, S.; D’Agostino, C.; Delfino, E.; Montella, A. From Manual to Automatic Pavement Distress Detection and Classification. In Proceedings of the 2017 5th IEEE International Conference on Models and Technologies for Intelligent Transportation Systems (MT-ITS), Naples, Italy, 26–28 June 2017; IEEE: Piscataway, NJ, USA, 2017; pp. 433–438.
10. Loprencipe, G.; de Almeida Filho, F.G.V.; de Oliveira, R.H.; Bruno, S. Validation of a Low-Cost Pavement Monitoring Inertial-Based System for Urban Road Networks. *Sensors* **2021**, *21*, 3127. [\[CrossRef\]](#)
11. Zakeri, H.; Nejad, F.M.; Fahimifar, A. Image Based Techniques for Crack Detection, Classification and Quantification in Asphalt Pavement: A Review. *Arch. Comput. Methods Eng.* **2017**, *24*, 935–977. [\[CrossRef\]](#)
12. Miśkiewicz, M.; Daszkiewicz, K.; Lachowicz, J.; Tysiac, P.; Jaskula, P.; Wilde, K. Nondestructive Methods Complemented by FEM Calculations in Diagnostics of Cracks in Bridge Approach Pavement. *Autom. Constr.* **2021**, *128*, 103753. [\[CrossRef\]](#)
13. Du, Z.; Yuan, J.; Xiao, F.; Hettiarachchi, C. Application of Image Technology on Pavement Distress Detection: A Review. *Measurement* **2021**, *184*, 109900. [\[CrossRef\]](#)
14. Mataei, B.; Nejad, F.M.; Zakeri, H. Automatic Pavement Texture Measurement Using a New 3D Image-Based Profiling System. *Measurement* **2022**, *199*, 111456. [\[CrossRef\]](#)
15. Saad, A.M.; Tahar, K.N. Identification of Rut and Pothole by Using Multicopter Unmanned Aerial Vehicle (UAV). *Measurement* **2019**, *137*, 647–654. [\[CrossRef\]](#)

16. Garilli, E.; Bruno, N.; Autelitano, F.; Roncella, R.; Giuliani, F. Automatic Detection of Stone Pavement's Pattern Based on UAV Photogrammetry. *Autom. Constr.* **2021**, *122*, 103477. [CrossRef]
17. Hoang, N.-D. Automatic Detection of Asphalt Pavement Raveling Using Image Texture Based Feature Extraction and Stochastic Gradient Descent Logistic Regression. *Autom. Constr.* **2019**, *105*, 102843. [CrossRef]
18. Abbondati, F.; Biancardo, S.A.; Veropalumbo, R.; Dell'Acqua, G. Surface Monitoring of Road Pavements Using Mobile Crowdsensing Technology. *Measurement* **2021**, *171*, 108763. [CrossRef]
19. Kheirati, A.; Golroo, A. Low-Cost Infrared-Based Pavement Roughness Data Acquisition for Low Volume Roads. *Autom. Constr.* **2020**, *119*, 103363. [CrossRef]
20. Sattar, S.; Li, S.; Chapman, M. Developing a near Real-Time Road Surface Anomaly Detection Approach for Road Surface Monitoring. *Measurement* **2021**, *185*, 109990. [CrossRef]
21. Ouma, Y.O.; Hahn, M. Pothole Detection on Asphalt Pavements from 2D-Colour Pothole Images Using Fuzzy c -Means Clustering and Morphological Reconstruction. *Autom. Constr.* **2017**, *83*, 196–211. [CrossRef]
22. Zhang, D.; Zou, Q.; Lin, H.; Xu, X.; He, L.; Gui, R.; Li, Q. Automatic Pavement Defect Detection Using 3D Laser Profiling Technology. *Autom. Constr.* **2018**, *96*, 350–365. [CrossRef]
23. Dan, D.; Dan, Q. Automatic Recognition of Surface Cracks in Bridges Based on 2D-APES and Mobile Machine Vision. *Measurement* **2021**, *168*, 108429. [CrossRef]
24. Li, G.; Liu, Q.; Ren, W.; Qiao, W.; Ma, B.; Wan, J. Automatic Recognition and Analysis System of Asphalt Pavement Cracks Using Interleaved Low-Rank Group Convolution Hybrid Deep Network and SegNet Fusing Dense Condition Random Field. *Measurement* **2021**, *170*, 108693. [CrossRef]
25. McNeil, S.; Humplick, F. Evaluation of Errors in Automated Pavement-Distress Data Acquisition. *J. Transp. Eng.* **1991**, *117*, 224–241. [CrossRef]
26. Dong, Q.; Chen, X.; Dong, S.; Ni, F. Data Analysis in Pavement Engineering: An Overview. *IEEE Trans. Intell. Transp. Syst.* **2022**, *23*, 22020–22039. [CrossRef]
27. Silyanov, V.V.; Sodikov, J.I.; Kiran, R.; Sadikov, A.I. An Overview Road Data Collection, Visualization, and Analysis from the Perspective of Developing Countries. *IOP Conf. Ser. Mater. Sci. Eng.* **2020**, *832*, 012056. [CrossRef]
28. Available online: <https://www.pavemetrics.com/applications/road-inspection/lcms2-en/> (accessed on 30 September 2022).
29. Pantuso, A.; Loprencipe, G.; Bonin, G.; Teltayev, B.B. Analysis of Pavement Condition Survey Data for Effective Implementation of a Network Level Pavement Management Program for Kazakhstan. *Sustainability* **2019**, *11*, 901. [CrossRef]
30. Tsai, Y.-C.J.; Li, F. Critical Assessment of Detecting Asphalt Pavement Cracks under Different Lighting and Low Intensity Contrast Conditions Using Emerging 3D Laser Technology. *J. Transp. Eng.* **2012**, *138*, 649–656. [CrossRef]
31. Laurent, J.; Hébert, J.F.; Lefebvre, D.; Savard, Y. High-Speed Network Level Road Texture Evaluation Using 1mm Resolution Transverse 3D Profiling Sensors Using a Digital Sand Patch Model. In Proceedings of the 7th International Conference on Maintenance and Rehabilitation of Pavements and Technological Control, Auckland, New Zealand, 28–30 August 2012; pp. 28–30.
32. Laurent, J.; Hébert, J.F.; Lefebvre, D.; Savard, Y. 3D Laser Road Profiling for the Automated Measurement of Road Surface Conditions and Geometry. In Proceedings of the 7th RILEM International Conference on Cracking in Pavements, Dordrecht, The Netherlands, 20–22 June 2012; Springer: Dordrecht, The Netherlands, 2012.
33. Sahhaf, S.A.; Rahimi, S. Investigation of Laser Systems Used in Pavement Management Systems (PMS). In Proceedings of the 8th National Congress on Civil Engineering, BabolNoshirvani University of Technology, Babol, Iran, 7–8 May 2014.
34. Laurent, J.; Lefebvre, D.; Samson, E. Development of a New 3D Transverse Laser Profiling System for the Automatic Measurement of Road Cracks. In Proceedings of the 6th Symposium on Pavement Surface Characteristics, Potoroz, Slovenia, 1 January 2008.
35. Li, Q.; Zhang, D.; Zou, Q.; Lin, H. 3D Laser Imaging and Sparse Points Grouping for Pavement Crack Detection. In Proceedings of the 2017 25th European Signal Processing Conference (EUSIPCO), Kos Island, Greece, 28 August–2 September 2017; pp. 2036–2040.
36. Laefer, D.F.; Truong-Hong, L.; Carr, H.; Singh, M. Crack Detection Limits in Unit Based Masonry with Terrestrial Laser Scanning. *NDT E Int.* **2014**, *62*, 66–76. [CrossRef]
37. Wix, R.; Leschinski, R. 3D Technology for Managing Pavements. In Proceedings of the International Public Works Conference, Brisbane, QLD, Australia, 27–29 March 2013.
38. Laurent, J.; Hébert, J.F.; Talbot, M. *Automated Detection of Sealed Cracks Using 2D and 3D Road Surface Data*; Pavemetrics Systems Inc.: Québec City, QC, Canada, 2010.
39. Mulry, B.; Jordan, M.; O'Brien, D.A. Automated Pavement Condition Assessment Using Laser Crack Measurement System (LCMS) on Airfield Pavements in Ireland. In Proceedings of the 9th International Conference on Managing Pavement Assets, Washington, DC, USA, 18–21 May 2015.
40. Williams, B.; Andre, N.; Bowey, K.; Huynh, K. Integrating Laser Crack Measuring System into the Saskatchewan Pavement Management System. In Proceedings of the TAC 2017: Investing in Transportation: Building Canada's Economy—2017 Conference and Exhibition of the Transportation Association of Canada, Labrador, NL, Canada, 24–27 September 2017.
41. Kroizer, A.; Routtenberg, T.; Eldar, Y.C. Bayesian Estimation of Graph Signals. *IEEE Trans. Signal Process.* **2022**, *70*, 2207–2223. [CrossRef]
42. Colonnese, S.; Lorenzo, P.D.; Cattai, T.; Scarano, G.; Fallani, F.D.V. A Joint Markov Model for Communities, Connectivity and Signals Defined Over Graphs. *IEEE Signal Process. Lett.* **2020**, *27*, 1160–1164. [CrossRef]

43. Pantuso, A.; Flintsch, G.W.; Katicha, S.W.; Loprencipe, G. Development of Network-Level Pavement Deterioration Curves Using the Linear Empirical Bayes Approach. *Int. J. Pavement Eng.* **2021**, *22*, 780–793. [[CrossRef](#)]
44. Doğan, G.; Ergen, B. A New Mobile Convolutional Neural Network-Based Approach for Pixel-Wise Road Surface Crack Detection. *Measurement* **2022**, *195*, 111119. [[CrossRef](#)]
45. Bonin, G.; Folino, N.; Loprencipe, G.; Oliverio Rossi, G.; Polizzotti, S.; Teltayev, B. Development of a Road Asset Management System in Kazakhstan. In Proceedings of the TIS 2017 International Congress on Transport Infrastructure and Systems, Rome, Italy, 10–12 April 2017; pp. 10–12.
46. Di Mascio, P.; Moretti, L. Implementation of a Pavement Management System for Maintenance and Rehabilitation of Airport Surfaces. *Case Stud. Constr. Mater.* **2019**, *11*, e00251. [[CrossRef](#)]
47. Canestrari, F.; Ingrassia, L.P. A Review of Top-down Cracking in Asphalt Pavements: Causes, Models, Experimental Tools and Future Challenges. *J. Traffic Transp. Eng.* **2020**, *7*, 541–572. [[CrossRef](#)]
48. Cation, K.A.; Shahin, M.Y.; Scullion, T.; Lytton, R.L. *Development of a Preventive Maintenance Algorithm for Use in Pavement Management Systems*; Transportation Research Board: Washington, DC, USA, 1987; pp. 1–11. ISBN 0-309-04503-7.
49. van de Schoot, R.; Depaoli, S.; King, R.; Kramer, B.; Märtens, K.; Tadesse, M.G.; Vannucci, M.; Gelman, A.; Veen, D.; Willemsen, J. Bayesian Statistics and Modelling. *Nat. Rev. Methods Primers* **2021**, *1*, 1–26. [[CrossRef](#)]
50. Cao, W.; Liu, Q.; He, Z. Review of Pavement Defect Detection Methods. *IEEE Access* **2020**, *8*, 14531–14544. [[CrossRef](#)]
51. Cano-Ortiz, S.; Pascual-Muñoz, P.; Castro-Fresno, D. Machine Learning Algorithms for Monitoring Pavement Performance. *Autom. Constr.* **2022**, *139*, 104309. [[CrossRef](#)]
52. Yao, L.; Leng, Z.; Jiang, J.; Ni, F. Modelling of pavement performance evolution considering uncertainty and interpretability: A machine learning based framework. *Int. J. Pavement Eng.* **2021**, 1–16. [[CrossRef](#)]
53. Jacovitti, G.; Panci, G.; Scarano, G. Bussgang-Zero Crossing Equalization: An Integrated HOS-SOS Approach. *IEEE Trans. Signal Process.* **2001**, *49*, 2798–2812. [[CrossRef](#)]
54. Panci, G.; Campisi, P.; Colonnese, S.; Scarano, G. Multichannel Blind Image Deconvolution Using the Bussgang Algorithm: Spatial and Multiresolution Approaches. *IEEE Trans. Image Process.* **2003**, *12*, 1324–1337. [[CrossRef](#)]
55. LeCam, L. On the Distribution of Sums of Independent Random Variables. In *Bernoulli 1713, Bayes 1763, Laplace 1813*; Springer: Berlin/Heidelberg, Germany, 1965; pp. 179–202.
56. Poor, H.V. *An Introduction to Signal Detection and Estimation*; Springer Science & Business Media: Boston, MA, USA, 2013; ISBN 1-4757-2341-5.
57. Hobza, T.; Pardo, L.; Vajda, I. Robust Median Estimator in Logistic Regression. *J. Stat. Plan. Inference* **2008**, *138*, 3822–3840. [[CrossRef](#)]
58. Loprencipe, G.; Pantuso, A. A Specified Procedure for Distress Identification and Assessment for Urban Road Surfaces Based on PCI. *Coatings* **2017**, *7*, 65. [[CrossRef](#)]